

Article

Fe₂O₃/MgFe₂O₄ Nanosheet on Nickel Foam for High-Performance Asymmetric Supercapacitors

Jiao Li ^{1,2}, Yilong Mei ², Qiwei Su ², Zhaoxin Wang ² and Guanlun Guo ^{2,*} ¹ The School of Arts, Hubei University of Education, Wuhan 430205, China² Hubei Key Laboratory of Advanced Technology for Automotive Components & Hubei Collaborative Innovation Center for Automotive Components Technology, Wuhan University of Technology, Wuhan 430070, China

* Correspondence: glguo@whut.edu.cn

Abstract: In this paper, the effects of nickel foam with different thicknesses, as a fluid collector, on the morphology and properties of electrode materials were explored. The Fe₂O₃ material, which is a common active material for supercapacitor electrodes, was used in combination with MgFe₂O₄. This combination resulted in better electrochemical performance and cycle stability for the Fe₂O₃ material. The synthesis ratio of Fe₂O₃/MgFe₂O₄ materials with the best stability, as reported in a previous article, was selected for this study. The electrode with the best performance was then selected and assembled with activated carbon to form an asymmetric supercapacitor. This supercapacitor exhibited a high specific capacity of 240 C/g, an energy density of 58.75 Wh/kg, and a power density of 200.4 W/kg at a current density of 1 A/g. These findings provide valuable references for the selection of different fluid collectors with electrodes.

Keywords: asymmetric supercapacitor; Fe₂O₃/MgFe₂O₄; collector

Citation: Li, J.; Mei, Y.; Su, Q.; Wang, Z.; Guo, G. Fe₂O₃/MgFe₂O₄ Nanosheet on Nickel Foam for High-Performance Asymmetric Supercapacitors. *Crystals* **2023**, *13*, 1561. <https://doi.org/10.3390/cryst13111561>

Academic Editor: Ravindra Bulakhe

Received: 8 October 2023

Revised: 24 October 2023

Accepted: 28 October 2023

Published: 1 November 2023



Copyright: © 2023 by the authors. Licensee MDPI, Basel, Switzerland. This article is an open access article distributed under the terms and conditions of the Creative Commons Attribution (CC BY) license (<https://creativecommons.org/licenses/by/4.0/>).

1. Introduction

As the most common secondary energy, energy storage technologies for electrical energy have been extensively researched. Among the large number of available energy storage technologies, the most promising are lithium-ion batteries and ultracapacitors. Supercapacitors fill the performance gap between batteries and capacitors by offering energy and power densities between them. They can store more energy than conventional capacitors and have a higher cycle life, a higher multiplier performance, and better stability than batteries. These advantages give supercapacitors a wide range of application scenarios and have attracted widespread interest. In the previous article [1], the Fe₂O₃/MgFe₂O₄ electrode was prepared using the hydrothermal method, which can achieve high specific capacity and good cycle stability. The electrochemical testing and material characterization revealed the synergistic effect of the two materials, and the reason for the improvement of electrode cycle stability was analyzed [2–5].

The choice of fluid collector in hydrothermal processes significantly impacts electrode performance as collector morphology affects material growth [6–9]. Prior research has examined nickel foam thickness and found that a common thickness of 0.3 mm yields Fe₂O₃ nanosheets and MgFe₂O₄ nanoparticles, which is important due to the increased active sites with a thicker foam. Therefore, the material choice and structure of fluid collectors are crucial as they have varying conductivity and oxidation resistance, which in turn influence overall electrode performance. Additionally, material structures and porosities also affect growth quality [10–13]. Wang et al. [14] used Fe₂O₃ nanotube arrays coated with polypyrrole on carbon cloth, which displayed good cyclic stability with 80% retention after 10,000 cycles. However, they achieved only a modest initial specific capacity of 230 F/cm² at 1 A/cm². In contrast, Kumar et al. [15] achieved a higher initial specific capacity of

600 F/g with $\text{Mn}_3\text{O}_4\text{-Fe}_2\text{O}_3/\text{Fe}_3\text{O}_4\text{@rGO}$, although only 61% was retained after 1000 cycles. Therefore, different carriers have a great influence on the performance of the electrode.

The previous article explored the optimal stability of the $\text{Fe}_2\text{O}_3/\text{MgFe}_2\text{O}_4$ material synthesis ratio. In this paper, the influence of nickel foam with different thicknesses, as a fluid collector, on the morphology and performance of electrode materials will be investigated using the synthesis ratio explored in the previous article, and the synthetic route of the material remains unchanged [1]. Nickel foam with different thicknesses will be used in the market common nickel foam. The electrode with the best performance will then be selected as the cathode. Taking into consideration factors such as potential window and specific capacity, the anode of the assembled supercapacitor will be commercial activated carbon [16,17].

2. Experimental Section

2.1. Preparation of $\text{Fe}_2\text{O}_3/\text{MgFe}_2\text{O}_4$ Powders

The steps for the synthesis of $\text{Fe}_2\text{O}_3/\text{MgFe}_2\text{O}_4$ electrode materials are the same as in the previous paper, except that different thicknesses of the nickel foam are changed as the carrier. $\text{Fe}_2\text{O}_3/\text{MgFe}_2\text{O}_4$ electrodes with 0.3, 0.5, and 1.0 mm thicknesses of nickel foam were prepared, respectively named FM-2, FM-0.5NF, and FM-1.0NF, and their properties were compared using electrochemical tests [18]. Then, the reasons for the performance changes were analyzed through the characterization of various materials. The specific parameters of the electrodes are shown in Table 1. The molar ratio of composites is calculated by the ion concentration of ICP-OES.

Table 1. Comparison of nickel foam samples with different thicknesses.

Sample	Content (mmol)		Thickness	$\text{Fe}_2\text{O}_3/\text{MgFe}_2\text{O}_4$ Proportion
	$\text{Fe}(\text{NO}_3)_3 \cdot 9\text{H}_2\text{O}$	$\text{Mg}(\text{NO}_3)_2 \cdot 6\text{H}_2\text{O}$		
FM-2	2	0.5	0.3 mm	1.9:1
FM-0.5NF	2	0.5	0.5 mm	1.4:1
FM-1.0NF	2	0.5	1.0 mm	1.1:1

2.2. Preparation of Anode Electrode

To prepare the anode materials for asymmetric supercapacitors, the fluid collecting nickel foam is first cleaned by ultrasound. Then, the foam is cut to the required shape and size. The cleaning process of the foam nickel involves sequentially using 1 M dilute hydrochloric acid, anhydrous ethanol, and deionized water for 3–5 min. This effectively removes the oxide layer, surface oil stains, and other impurities. After the cleaning, the nickel foam is placed in a vacuum drying oven. Vacuuming is conducted, followed by heating the foam up to 60 °C at a heating rate of 2 °C/min. The heating is maintained at 60 °C for 6 h. The mixture consists of GO, ACET, and PVDF in a ratio of 8:1:1. 1-methyl-2-pyrrolidone is then slowly dripped until the powder is fully wet. The evenly coated mixture is applied to both sides of the nickel foam using a brush and is dried for 6 h. Subsequently, the nickel foam is pressed by a tablet press at a pressure of 10 MPa for 5 min. This process ensures that the electrode material is firmly packed into the pores of the nickel foam, resulting in the GO electrode. By comparing the weight of the nickel foam before and after the electrode, the load of active material is determined to be 2–4 mg/cm² [19–22].

2.3. Materials Characterisation and Electrochemical Measurements

For the preparation, all samples were analyzed in phase by X-ray diffraction (XRD, Bruker D8 Advance, Wuhan, China). The product morphology was characterized using a scanning electron microscope (SEM, Zeiss Gemini 300, Wuhan, China). Chemical composition and material binding mode samples were characterized using transmission electron microscopy (TEM, Tecnai G2 F30, Wuhan, China). A full spectral characterization of the sample and the analysis of the $\text{Fe}^{2+}/\text{Fe}^{3+}$ content of samples before and after cycle

testing were characterized using X-ray photoelectron spectroscopy (XPS, Thermo Scientific K-Alpha, Wuhan, China).

The electrochemical properties of all samples were tested using a three-electrode system with the sample electrode as the working electrode, the platinum wire as the counter electrode, the Hg/HgO as the reference electrode, and the electrolyte using 1 M KOH. Cyclic voltammetry (CV), constant current charge/discharge and cyclic stability tests were carried out on all samples. The GCD test is used to calculate the specific capacity and is based on the following equation [23]:

$$C = \frac{I\Delta t}{m} \quad (1)$$

where C (C/g) is the specific capacity, I (A) is the discharge current, Δt (s) is the total discharge time, and m (mg) is the electrode material loading mass. The material loading masses were found using inductively coupled plasma optical emission spectrometer (ICP-OES) testing and ranged from 1.0 mg to 1.2 mg.

3. Results and Discussion

3.1. Phase Composition, Microstructure and Surface Chemistry

Figure 1 shows the XRD characterization of FM-2-0.5NF- and FM-2-1.0NF-loaded materials compared with FM-2 samples. As can be seen from the figure, the sample loads all have obvious diffraction peaks, which proves that the crystal structure is intact. Through comparison, it can be found that, for FM-0 sample load material [1], these peaks at 2θ angles of 24.125° , 33.117° , 35.604° , 40.823° , 49.412° , 54.002° , 62.375° , and 63.948° can be observed in the X-ray diffraction pattern, it is completely consistent with the standard card JCPDS NO.89-0597 of Fe_2O_3 material. For FM-2--0.5NF and FM-2-1.0NF samples, there are diffraction peaks at $2\theta = 30.212^\circ$, 35.587° , 37.227° , 43.253° , 57.210° , and 43.253° . The MgFe_2O_4 material standard card JCPDS NO.73-1960 is consistent with that of the FM-2 sample, and the intensity of these peaks relative to Fe_2O_3 diffraction peaks is greater than that of the FM-2 sample. From a certain level, it can be shown that the MgFe_2O_4 content in these samples accounts for a larger proportion [24,25].

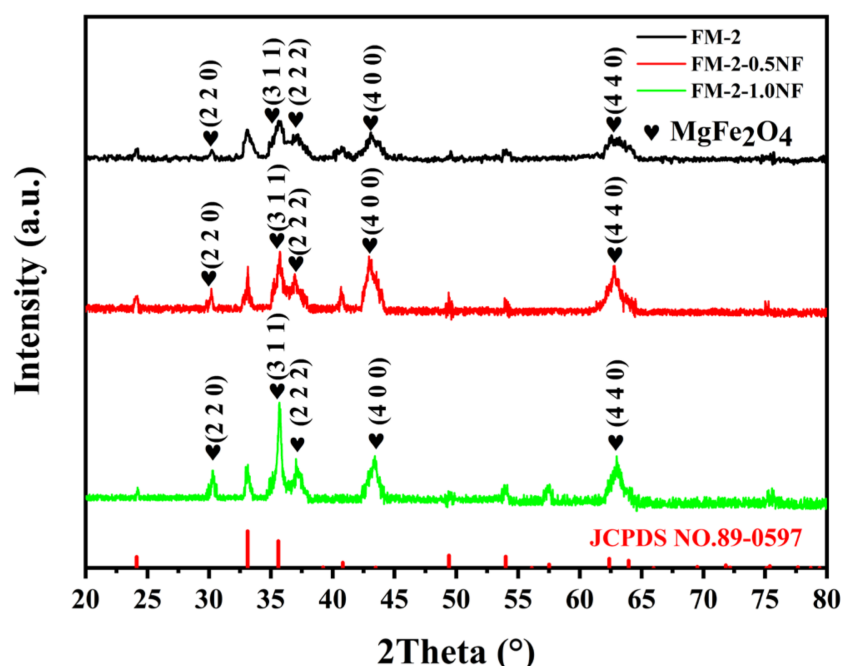


Figure 1. XRD pattern of FM-0.3 NF, FM-0.5 NF, and FM-1.0 NF.

X-ray photoelectron spectroscopy analysis was performed on FM-2-0.5NF and FM-2-1.0NF electrodes. The broad spectrum scanning patterns of samples in the range of 0–1400 eV are shown in Figure 2. As can be seen from the figure, in the binding energy range of 0–1400 eV, similar to the FM-2 sample, the spectra of C 1s, O 1s, Fe 2p, Ni 2p, and Mg 1s can also be clearly observed. The diffraction peak intensity of Mg 1s increases with the increase of nickel foam thickness, which indicates that the relative content of Mg increases to a certain extent, which is consistent with the change of molar ratio of $\text{Fe}_2\text{O}_3/\text{MgFe}_2\text{O}_4$ and the peak intensity of XRD obtained by the ICP-OES test. XRD and XPS wide-scan test patterns further show that $\text{Fe}_2\text{O}_3/\text{MgFe}_2\text{O}_4$ loaded in FM-2-0.5NF and FM-2-1.0NF samples have been successfully synthesized.

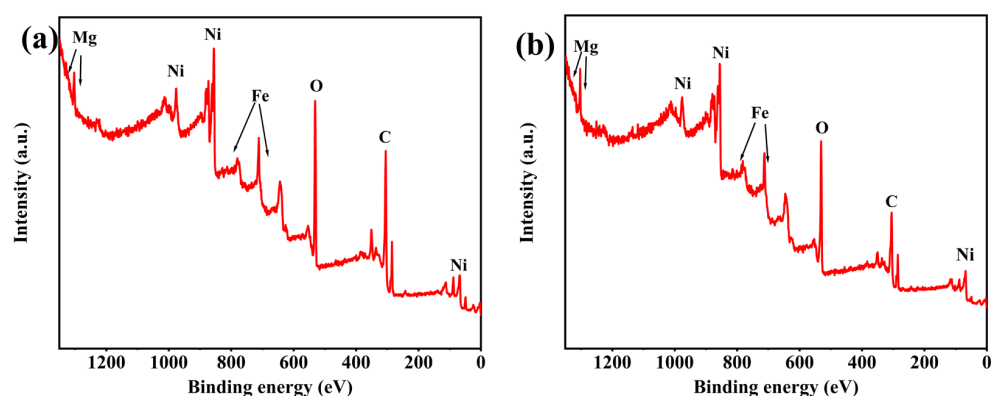


Figure 2. X-ray photoelectron spectroscopy for broad spectrum analysis. (a) FM-0.5NF (b) FM-1.0NF.

Figure 3 shows the SEM characterization of FM-0.5NF and FM-1.0NF. As can be seen from the figure, the supporting material morphology prepared by nickel foam with thicknesses of 0.5 and 1.0 mm under the same initial conditions is similar to that obtained by nickel foam with a thickness of 0.3 mm, both of which are the composite of nanosheets and nanoparticles. Figure 3a,c show the SEM images of FM-0.5NF and FM-1.0NF samples at 10,000 ratios, where the load material of the FM-2-1.0NF sample grows more densely, which is consistent with the conclusion that the load material of the FM-2-1.0NF sample is heavier by ICP-OES. The growth of both materials is relatively uniform, and there is no obvious agglomeration of nanosheets. Figure 3b,d shows the SEM characterization of 100,000 times of the two samples, in which the spherical substances in both samples are significantly increased and the gaps of the Fe_2O_3 nanosheets are filled in, indicating that, under the same initial preparation conditions, the MgFe_2O_4 material on the growth is significantly increased with a larger thickness of nickel foam as the base. Although the thicker nickel foam brings more growth sites of materials and increases the load material, the size of Fe_2O_3 nanosheets does not increase accordingly, and the thickness remains about 15 nm, similar to that of the MF-2 sample. The retention of the Fe_2O_3 nanosheet in a small size makes it less affected by volume change, which is also conducive to the retention of performance. More spherical MgFe_2O_4 increases the contact between Fe_2O_3 nanosheets, which may be helpful for electron conduction to some extent, while enhancing the electron exchange ability of the material. FM-0.5NF and FM-2-1.0NF have better stability than FM-2. According to SEM characterization, compared with FM-2 samples, FM-0.5NF and FM-1.0NF samples can support more MgFe_2O_4 material, and more material loading does not increase the size of Fe_2O_3 nanosheets. This makes the contact between $\text{Fe}_2\text{O}_3/\text{MgFe}_2\text{O}_4$ materials better, thus enhancing the electron exchange and further improving the stability of the material, which is also the reason for the retention of the electrochemical impedance of the material [26].

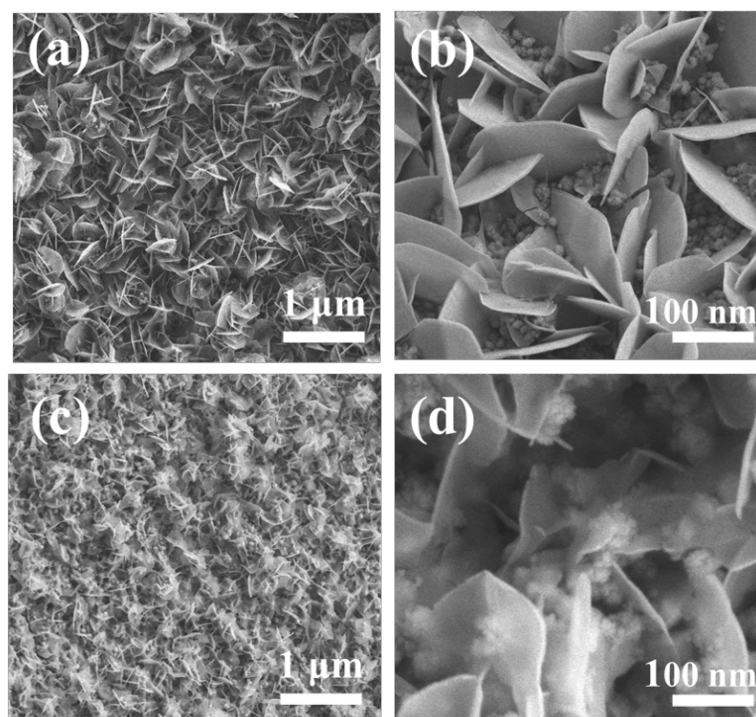


Figure 3. (a,b) FM-0.5NF sample FESEM (c,d) FM-1.0NF sample FESEM.

3.2. Electrochemical Characterizations

Electrochemical tests were conducted on FM-2-0.5NF and FM-2-1.0NF, and the results are shown in Figures 4 and 5. Figure 4a,b show the CV patterns of FM-2-0.5NF and FM-2-1.0NF at a scanning rate of 10–50 mV/s. Both electrodes have obvious REDOX peaks, showing pseudocapacitance. The reduction peak has a large response current, but the current magnitude is different from the peak current of the oxidation peak, showing a quasi-reversible reaction. The CV patterns of FM-2-0.5NF and FM-2-1.0NF samples vary with the scanning rate, and the shape and position of the REDOX peaks are still well maintained. For FM-2-0.5NF samples, at a scanning rate of 10 mV/s, the oxidation peak and reduction peak potentials are 0.47 V and 0.36 V, respectively, with a difference of 0.11 V. At a scanning rate of 50 mV/s, they were offset to 0.60 V and 0.33 V, respectively, and the difference increased to 0.27 V. At 10mV/s, the reduction peaks of FM-2-1.0NF samples were 0.5 V and 0.32 V, respectively, with a difference of 0.18 V; at 50 mV/s, they were 0.55 V and 0.29 V, with a difference of 0.26 V. The results show that both 0.5 mm and 1.0 mm thick nickel foam electrodes have good reversibility, and 1.0 mm nickel foam electrodes have better reversibility. Figure 4c,d show the GCD patterns of FM-2-0.5NF and FM-2-1.0NF. A 1–8 A/g current density was also selected for each constant-current charge–discharge test. As can be seen from the figure, the specific capacity of FM-2-0.5NF and FM-2-1.0NF samples decreases with the increase of current density. At a 1 A/g current density, the specific capacity is 372.5 C/g and 379.5 C/g, respectively, which is slightly reduced compared with the FM-2 sample. Among them, FM-2-1.0NF samples have a better magnification performance than FM-2-0.5NF samples. At a 1–8 A/g current density, the specific capacities are 379, 348.5, 327.5, and 291 C/g, respectively. When the current density reaches a high magnification of 8 A/g, the specific capacitors can still reach 77% of the specific capacitors when the current density is 1 A/g, 67% higher than FM-2-0.5NF and 73% higher than FM-2. Since the electrolyte is used consistently, this increase in magnification performance may be due to load material variations. Among them, the FM-0.5-NF sample has the lowest specific capacity, which may be due to the fact that 0.5 mm nickel foam does not have advantages for the growth of materials. Further analysis was conducted through subsequent tests and characterization.

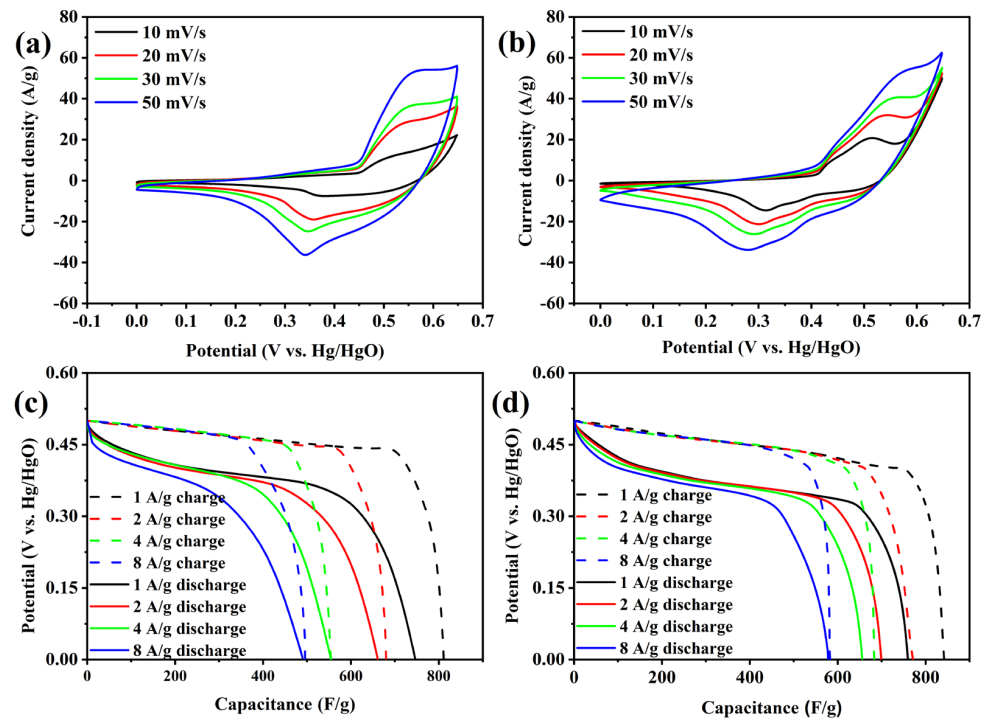


Figure 4. CV curves of (a,b) FM-2-0.5NF and FM-2-1.0NF and GCD curves of (c,d) FM-2-0.5NF and FM-2-1.0NF.

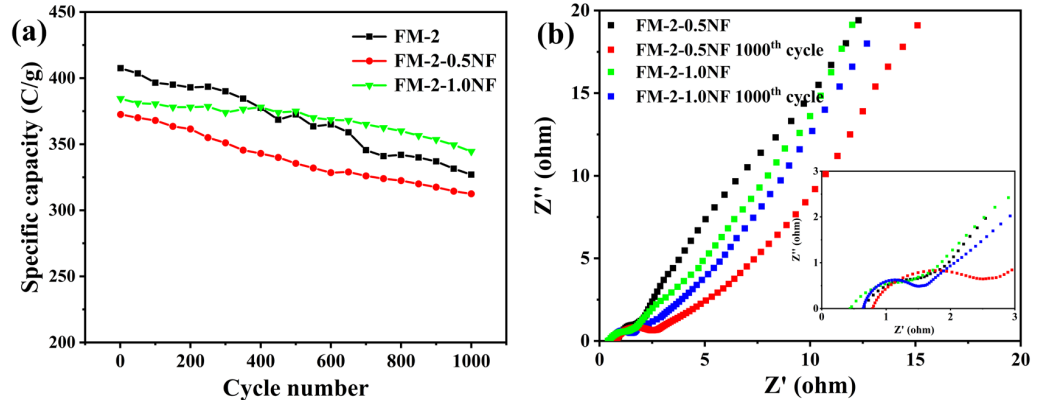


Figure 5. (a) FM-0.5NF and FM-1.0NF cyclic stability patterns (b) FM-0.5NF and FM-1.0NF cyclic EIS patterns.

Figure 5a depicts the cyclic stability pattern of FM-2, Fm-2-0.5 NF, and Fm-2-1.0 NF. It can be observed that the overall specific capacity of FM-2-0.5NF and FM-2-1.0NF decreases during the cycle. After the GCD cycle, the specific capacity of FM-2-0.5NF declines to 312.5 C/g, which is 83.9% of the initial specific capacity. In comparison, the specific capacity of the FM-5 sample after the cycle is 344.5 C/g. This confirms that the Fm-2-1.0 NF sample exhibits a slower decay rate, indicating an increase in the thickness of the nickel foam and a decrease in the initial specific capacity of the hydrothermal electrode. However, this trade-off leads to improved cycle stability. Furthermore, even though the specific capacity of FM-2-1.0NF is initially slightly lower than that of FM-2, it consistently remains at 375.5 C/g after approximately 400 cycles, which is consistently higher than the FM-2 sample. The improved stability can be attributed to the larger size and pore size of the nickel foam. On the other hand, Figure 5b shows the electrochemical impedance curves before and after the FM-2-0.5NF and FM-2-1.0NF cycles, and Table 2 lists the results of the

electrical conductivity test. Prior to the cycle, FM-2-0.5NF, FM-2-1.0NF samples exhibited Faraday impedance of 1.1 Ω and 0.6 Ω , and the exhibit electrical conductivity values of 1429 s/cm and 1250 s/cm, respectively, with FM-2-1.0NF samples having the lowest initial impedance. After 1000 cycles for both electrodes, the Faraday impedance increased to 1.7 Ω for the FM-2-0.5NF sample and 0.9 Ω for the FM-2-1.0NF sample. These results suggest that the 1.0 mm nickel foam electrode has the lowest impedance after circulation, representing the minimal degree of material deactivation and, hence, the best stability.

Table 2. The conductivity results of the sample.

Sample	Thickness (mm)	Resistivity (m Ω ·cm)	Conductivity (s/cm)
FM-2	0.326	0.2	5000
FM-2-0.5NF	0.532	0.7	1429
FM-2-1.0NF	1.028	0.8	1250

Figure 6 shows the XPS characterization pattern before and after FM-2-0.5NF and FM-2-1.0NF cycles. Figure 6a shows the O 1s spectra of FM-2-0.5NF and FM-2-1.0NF before and after the cycle. All curves can also be fitted to three components corresponding to lattice oxygen (O_I), chemisorbed oxygen (O_{II}), and physical adsorption oxygen (O_{III}), which are similar to FM-0 and FM-2. The content of the three oxygen elements is shown in Figure 6b. It can be seen from the figure that the chemisorbed oxygen ratio of FM-2-1.0NF after cycling is higher than that of FM-2-0.5NF, indicating that the FM-2-1.0NF electrode has better activity. The chemisorption oxygen ratio of FM-2-0.5NF and FM-2-1.0NF decreased after 1000 cycles, and the initial O_{II} percentage of FM-2-1.0NF was about 61%, which remained at 68% after 1000 cycles. However, the chemisorbed oxygen ratio of FM-2-0.5NF samples decreased significantly before and after the cyclic charge-discharge test, accounting for 33% after the cycle, which was the lowest among the four samples. Therefore, it can be inferred that FM-2-1.0NF electrode materials have more oxygen vacancies at the initial stage and have the best electrochemical activity [27,28].

Figure 6c,d shows the spectrum of Fe2p before and after the cycle of the FM-2-1.0NF sample. It can be seen from the figure that Fe2p has two different characteristic peaks at 710.8 eV and 724.4 eV, which can correspond to the peaks of Fe 2p_{3/2} and Fe 2p_{1/2}. The location of the peak value can correspond to that of the FM-2 sample. After partial peak fitting, FM-2-0.5NF samples had a relatively high Fe^{2+}/Fe^{3+} ratio of 1.19 before the cycle. After 1000 cycles, Fe^{2+}/Fe^{3+} decreased to 0.68, indicating a loss of material activity, which was also consistent with the assumption of oxygen vacancy. Figure 6c,d show the Fe 2p spectra of FM-2-1.0NF samples before and after cycling. Before the cycle, Fe^{2+}/Fe^{3+} was 1.1 and, after the cycle, it remained at 0.94, indicating that FM-2-1.0NF samples had better activity preservation, which was due to the better reversible reaction during the charging and discharging process [29].

A larger thickness of nickel foam will have more material forming sites. Therefore, these sites will increase the overall load of the material, but they will not have a significant impact on the nanometer size of the material. The electrode prepared by nickel foam with a 0.5 mm thickness has a similar growth material proportion and mass compared to 0.3 mm, but its conductivity is greatly reduced. On the other hand, the conductivity of the electrode prepared with 1.0 mm thick nickel foam is similar, but the quality and proportion of the material is lower, indicating that 0.5 mm thick nickel foam does not offer any advantage. Although the 1.0 mm thickness of nickel foam exhibits worse conductivity, it provides better contact between the composites, leading to lower electrochemical impedance and better stability. Thus, the initial specific capacity of the FM-2-1.0NF sample is smaller, but the retention rate of the capacitor is better during cycling. Consequently, in this follow-up study, the FM-2-1.0NF electrode prepared with foam nickel of a 1.0mm thickness was chosen as the research choice [30].

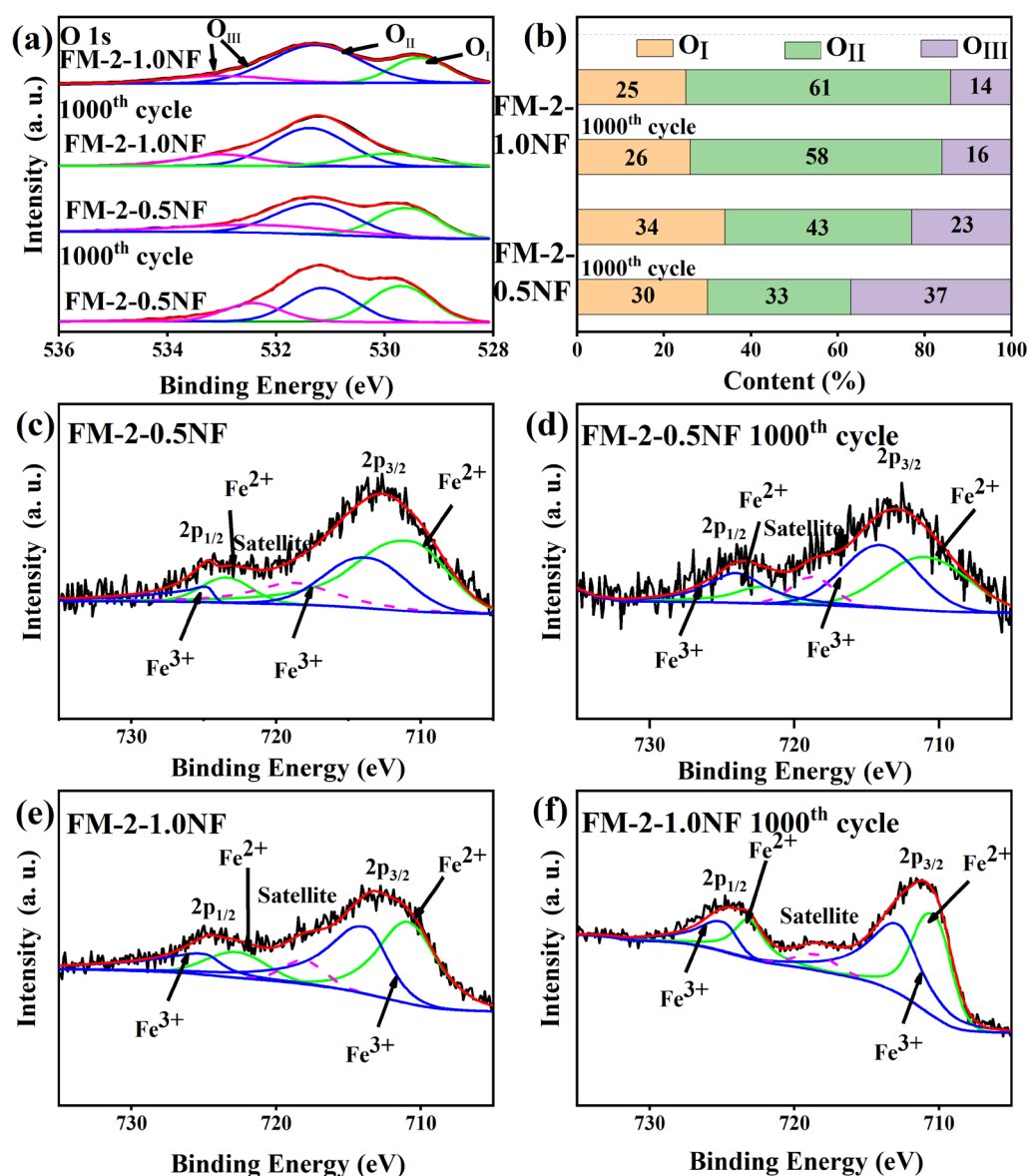


Figure 6. (a) XPS spectrum of O1s (b) contents of O_I, O_{II}, and O_{III} before and after cycle (c,d) Fe 2p spectrum of FM-2-0.5NF before and after cycle (e,f) Fe 2p spectrum of FM-2-1.0NF before and after cycle.

The GO electrode was tested. The cyclic voltammetry test pattern is shown in Figure 7a. As can be seen from the figure, at a low scanning rate, the CV pattern is close to a rectangle, showing double electric layer capacitance dominated by physical adsorption. The shape of the rectangle is irregular, indicating the existence of a REDOX reaction, which may be attributed to the functional groups on the GO surface. At the scanning rate of 10–30 mV/s, the shape of the CV pattern remains basically unchanged, showing good magnification performance. When the scanning rate reaches 50 mV/s, part of the shape changes due to the great influence of the functional group pseudo-capacitance, but the shape is very symmetrical, indicating good reversibility. Figure 7b shows the comparison of CV patterns of the GO anode and the Fe₂O₃/MgFe₂O₄ electrode at a scanning rate of 10 mV/s. It can be found that the reduction peak of the GO electrode as an anode is higher, which is slightly lower than that of the cathode, but can be compensated by the increase of load mass.

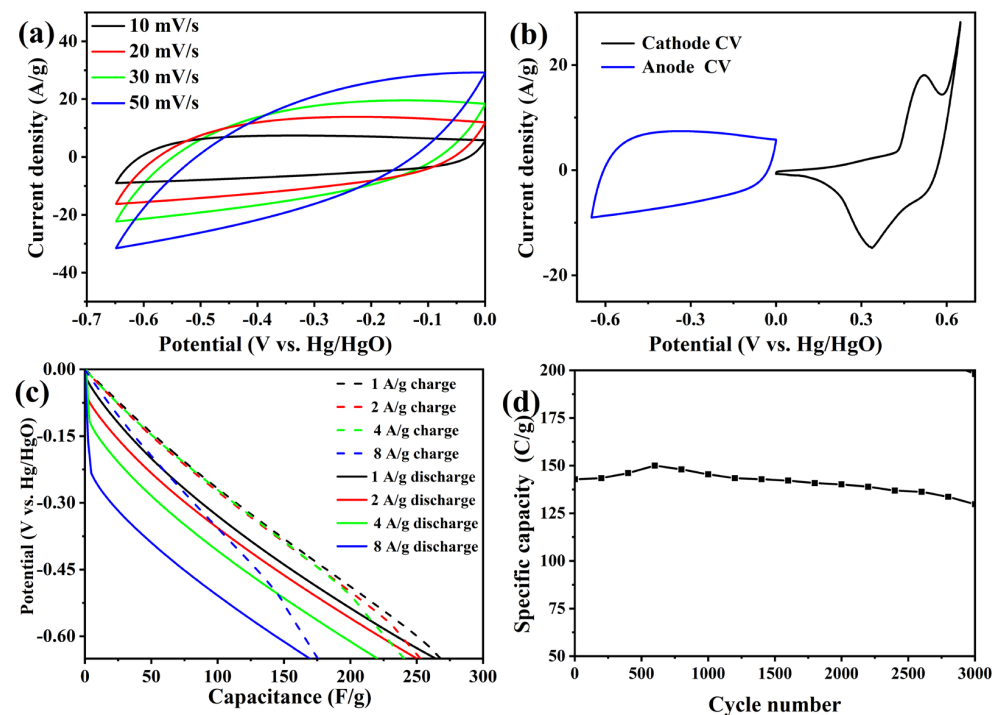


Figure 7. (a) CV curve of GO (b) CV comparison between GO anode and $\text{Fe}_2\text{O}_3/\text{MgFe}_2\text{O}_4$ cathode (c) GCD curve of GO (d) cyclic stability pattern of GO.

Figure 7c shows the GCD curve of the GO anode at $-0.65-0$ V. The curve is basically straight, with only a slight stagnation platform, showing obvious double-layer characteristics. The charge and discharge curve has a certain curvature, which comes from the pseudo capacitance of functional groups. At a high scanning rate, the Faraday response is delayed due to fast scanning, which leads to rapid potential change in the charge–discharge curve. At a current density of 1, 2, 4, and 8 A/g, the specific capacity of the electrode is 169.6, 160.5, 140.4, and 107.25 C/g respectively, which has a good performance. Figure 7d shows the cycle stability pattern of the GO electrode. The electrode increases slightly from 141.7 C/g to 148.85 C/g at 0–500 cycles, due to the exposure of more active sites during the cycle. After 3000 cycles, the electrode specific capacity drops to 127.4 C/g, which is 90% of the initial specific capacity. GO electrodes show good cyclic stability.

The electrochemical test shows that graphene oxide, as an anode, has a good double layer performance at $-0.65-0$ V potential and less pseudo capacitance performance. In the 1 A/g GCD test, it can show a high specific capacity of 169.6 C/g, and the GO electrode has good cyclic stability. After 3000 cycles, 90% of the initial specific capacity can be maintained. The electrode and $\text{Fe}_2\text{O}_3/\text{MgFe}_2\text{O}_4$ cathode can be adapted for the assembly of capacitor batteries.

The potential size of the whole battery is determined by the potential window of the anode and the cathode and the degree of adaptation of the poles. In this whole battery, because the anode uses the graphene oxide electrode, it has a large potential window. The cathode $\text{Fe}_2\text{O}_3/\text{MgFe}_2\text{O}_4$ electrode potential window is 0–0.65 V. In order to adapt the cathode potential, the anode potential window is first selected as $-0.65-0$ V. Therefore, the potential window of the whole battery is tested from 0–1.3 V, and the potential window is successively increased, and the appropriate working potential is selected based on specific capacity, charging, and discharging efficiency and other factors.

Figure 7 shows CV patterns and GCD patterns of different potentials of the whole battery at a scanning rate of 10 mV/s. Figure 8a shows the CV patterns of the whole battery with the maximum potential of 1.3–1.7 V. It can be seen from the figure that all CV patterns have obvious REDOX peaks with similar peak current heights, showing good reversibility. With the increase of the potential window, the response current also increased gradually,

and the CV pattern shifted to the right and maintained a good shape. In the pattern of the highest potential 1.3–1.7 V, the peak current density of the reduction peak is 5.55, 5.56, 6.15, 6.24, and 6.52 A/g, respectively. It can be seen that the circuit density of the reduction peak increases the most when the potential window reaches 0–1.5 V, indicating that the material activity increases greatly in this potential window. When the maximum potential reaches 1.7 V, it can be seen that the CV pattern has a large tail, which is due to the severe polarization caused by excessive potential. This polarization will cause electrolytic water reaction and damage to the electrode, so the maximum potential is limited below 1.7 V.

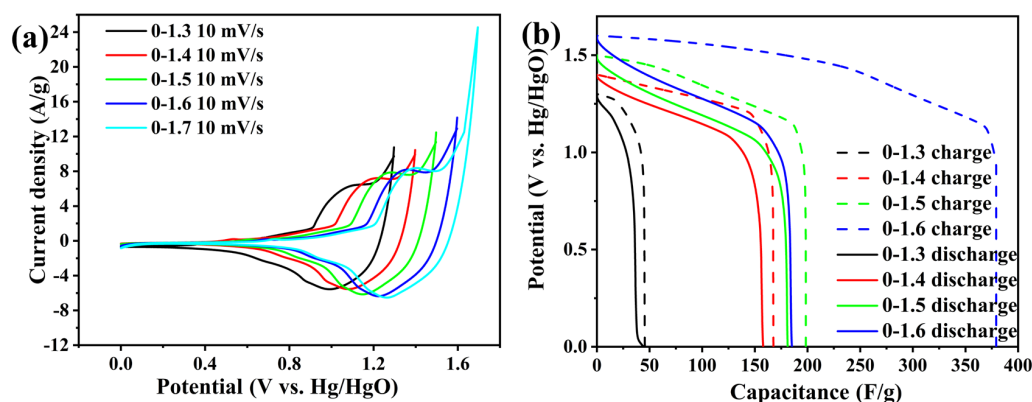


Figure 8. (a) CV patterns of different potential windows of the whole battery. (b) GCD patterns of different potential windows of the whole battery.

Figure 8b shows the GCD at a 1 A/g current density in different potential windows. It can be seen from the CV pattern that the maximum potential is limited to 1.7 V, so the maximum potential from 1.3 V to 1.6 V is selected. As can be seen from the figure, the charge–discharge capacitance increases with the increase of the potential window. In the 0–1.3 V potential window, the material exhibits low activity, with a specific capacity of 63.7 C/g. When the potential window expanded to 0–1.4 V, an obvious plateau of pattern stagnation was observed, indicating the occurrence of the Faraday reaction. The charging specific capacity is increased to 233.8 C/g, while the discharge specific capacity reaches 219.8 C/g, and the charging and discharging efficiency is 94%. When the potential window is 0–1.5 V, the charge–discharge capacitance is further increased, the charge–discharge specific capacity is 297 C/g, the discharge specific capacity is 241.5 C/g, and the charge–discharge efficiency drops slightly to 91%. When the potential window reaches 0–1.6 V, it can be found that the charge–discharge pattern has a serious stagnant platform. The charging specific capacity reaches 606.4 C/g, but the discharge specific capacity is still only 296 C/g, and the charge–discharge efficiency is only 49%. Excessive potential leads to difficulty in charging the electrode after reaching a certain potential, resulting in severe polarization of the electrode, and an irreversible Faraday reaction, releasing the same amount of electricity as the charged amount. Such high potential can cause serious deactivation of electrode material, damage of material morphology, and a decrease of electrode performance. Therefore, in order to take into account the specific capacity, charge–discharge efficiency, and electrode stability of the electrode, a potential window of 0–1.5 V was selected in this study.

Figure 9c shows that the supercapacitor exhibits the highest energy density, measuring 58.75 Wh/kg, at a current density of 1 A/g. Additionally, the power density is recorded at 200.4 W/kg. As the current density increases, it results in a reduction in charging and discharging time, leading to a substantial increase in power density but a decrease in energy density. The energy density–power density curve presented in the figure indicates a slight downward trend, illustrating the overall magnification performance of supercapacitors.

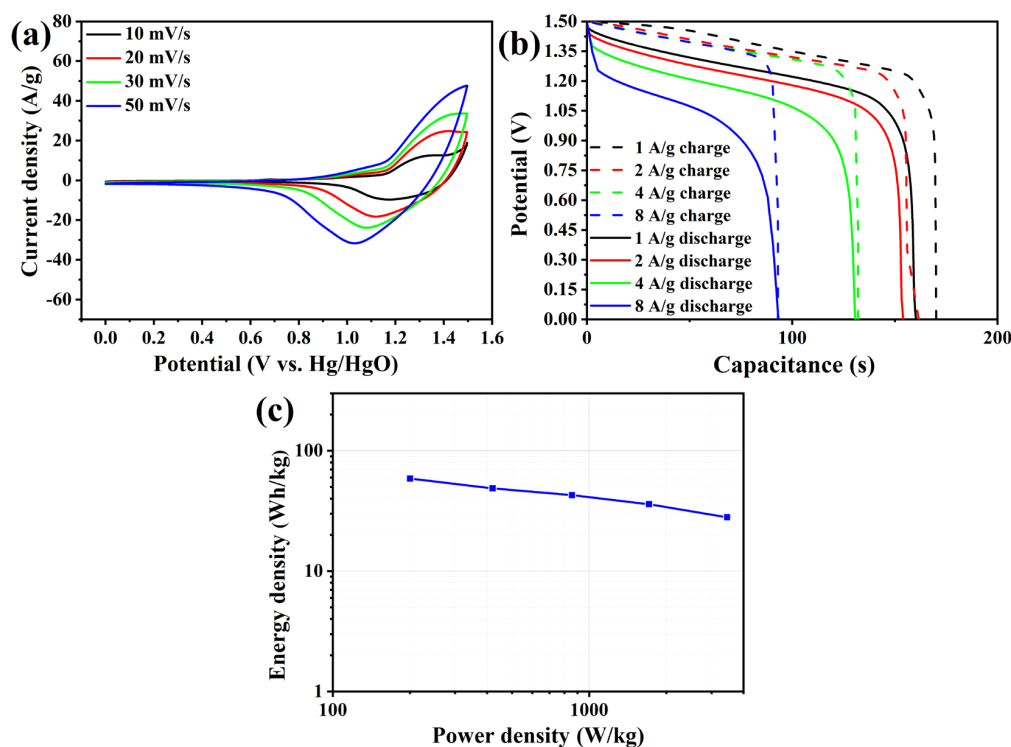


Figure 9. Full cell electrochemical test. (a) CV pattern. (b) GCD pattern. (c) Energy density–power density diagram.

It can be observed from Figure 9c that the supercapacitor exhibits the highest energy density of 58.75 Wh/kg at a current density of 1 A/g, along with a power density of 200.4 W/kg. As the current density increases, the charging and discharging time decreases, leading to a significant increase in power density but a decrease in energy density. The energy density–power density curve in the figure demonstrates a slight downward trend, reflecting the overall performance characteristics of supercapacitors.

The cycle stability pattern of the whole battery for 3000 cycles is shown in Figure 10a. It can be observed that the supercapacitor demonstrates good cycle stability. The specific capacity is maintained at 222 C/g, which is 92% of the initial specific capacity, after 1000 cycles. After 2000 cycles, the specific capacity decreases to 216 C/g, accounting for 90% of the initial specific capacity. Moreover, during the period from 2000 to 3000 cycles, the supercapacitors experience a faster decay in specific capacity. The specific capacity after 3000 cycles is 198 C/g, which corresponds to 83% of the initial specific capacity. Comparatively, the cycle stability of the whole battery of the supercapacitor is better than that of the cathode. This is attributed to two factors. Firstly, the high stability of the anode contributes to an improvement in the overall battery stability. Secondly, the presence of errors in the adaptation between the anode and cathode limits the utilization of the cathode material's activity, thereby enhancing the electrode's lifespan. Figure 10b shows the CV curve changes after different cycles. It can be seen from the figure that the electrode has the maximum response current density before the cycle starts, indicating that the supercapacitor has the best activity before the cycle. After 1000 cycles, the REDOX peak height of CV patterns decreased slightly, indicating partial deactivation of the material. By comparing with the reduction peak of the pre-cycle pattern, it can be found that the reduction peak of the supercapacitor decreases significantly at the potential range of 1.1–1.4 V, indicating that the supercapacitor is first deactivated from this range at the beginning of the cycle. After 2000 cycles, it can be found that the CV pattern does not change much compared with 1000 cycles, indicating that the loss of electrochemical activity is small. This conclusion can correspond to Figure 10a. According to the cycle stability pattern, the specific capacity decreases by only 6 C/g after 1000 cycles. After

3000 cycles, compared with CV patterns of 2000 cycles, it can be seen that the reduction peak value decreased significantly in the range of 0.8–1.1 V potential, while there was little change in the range of 1.1–1.4 V. This indicates that, in the late cycle, the supercapacitor was seriously deactivated at 0.8–1.1 V potential, while the activity of 1.1–1.4 V potential basically no longer declined. The sequence of deactivation may be related to the time of deactivation of the two materials in $\text{Fe}_2\text{O}_3/\text{MgFe}_2\text{O}_4$, respectively [31,32].

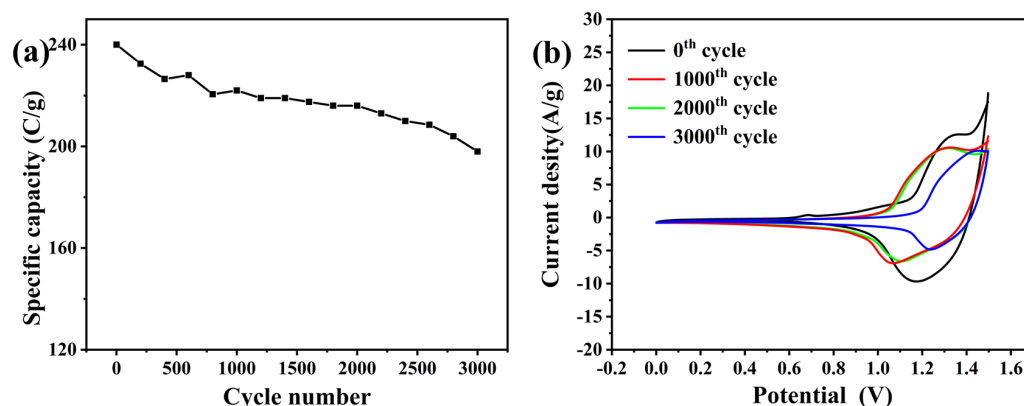


Figure 10. (a) Cycle stability curve of the whole battery of the supercapacitor. (b) CV pattern after different cycles.

By selecting appropriate cathodes for $\text{Fe}_2\text{O}_3/\text{MgFe}_2\text{O}_4$ electrodes and performing performance tests in a two-electrode system, it is found that the whole battery has a high specific capacity of 240 C/g, an energy density of 58.75 Wh/kg, and a power density of 200.4 W/kg at a current density of 1 A/g. The asymmetric supercapacitor composed of $\text{Fe}_2\text{O}_3/\text{MgFe}_2\text{O}_4//\text{GO}$ has a good electrochemical performance and can be used as a cheap and high-performance energy storage device.

4. Conclusions

The influence of the fluid collector on the active material and the performance of the electrode sheet in an electrode sheet is investigated in this study. The $\text{Fe}_2\text{O}_3/\text{MgFe}_2\text{O}_4$ material mentioned earlier is loaded onto various fluid collectors. Through electrochemical testing and material characterization, the impact of the fluid collector is examined, and a suitable fluid collector is chosen for electrode preparation. Subsequently, the obtained electrode serves as the cathode, and a suitable GO anode is selected. These components are then assembled into a hybrid supercapacitor battery. To obtain the parameters of the entire battery, appropriate potential window selection and thorough electrochemical testing are conducted. The following specific results are obtained:

- (1) After selecting the appropriate cathode electrode material, select the appropriate collector for it. $\text{Fe}_2\text{O}_3/\text{MgFe}_2\text{O}_4$ electrodes were prepared from nickel foam with different thicknesses, and the influence of different fluid concentrations was investigated by electrochemical testing and material characterization. It is found that, for electrodes, the larger thickness of nickel foam has more material forming sites, so the electrode load increases, but the larger load does not lead to the larger size of Fe_2O_3 nanosheets. In addition, the content of MgFe_2O_4 nanoparticles increased with the increase of thickness, indicating that more forming sites were convenient for the growth of MgFe_2O_4 nanoparticles. The addition of MgFe_2O_4 nanoparticles leads to better interstitial contact, thus improving electrochemical impedance and increasing the reversibility of the material reaction. Although the larger thickness of the nickel foam leads to poorer conductivity and thus lower initial specific capacity, combined with stability analysis, the larger-thickness nickel foam electrode has a better overall performance.

- (2) $\text{Fe}_2\text{O}_3/\text{MgFe}_2\text{O}_4$ electrodes were prepared by an appropriate collecting system as the cathode of the supercapacitor, and an appropriate anode was selected for it. It is found that the potential window of the electrode material is too narrow to be used as an anode. GO was selected as the anode with high performance. The electrode has a high specific capacity of 169.6 C/g and an excellent stability of 90% capacitance retention rate after 3000 cycles. Taking the electrode as the anode, the quality of active material was matched by the performance difference of the anode and cathode, and the whole battery of the supercapacitor was assembled.
- (3) An electrochemical test was carried out on the assembled full battery of the supercapacitor in the two-electrode system. Firstly, the specific capacity and charge–discharge efficiency of the electrode under different potential windows were selected as 0–1.5 V, and the test showed that the supercapacitor had a high specific capacity of 240 C/g at the current density of 1 A/g, energy density of 58.75 Wh/kg, and power density of 200.4 W/kg. Supercapacitors also have good stability, with an 83% capacitance retention rate for 3000 cycles. The deactivation potential sequence of the supercapacitor was analyzed by the CV curve after the cycle, and the difference of the deactivation process of the cathode composite material was determined.

This paper provides an idea for the selection of the $\text{Fe}_2\text{O}_3/\text{MgFe}_2\text{O}_4$ fluid set, and the assembled high performance $\text{Fe}_2\text{O}_3/\text{MgFe}_2\text{O}_4//\text{GO}$ asymmetric supercapacitor has good commercial value.

Author Contributions: Writing-original draft, J.L.; Writing-review and editing, Y.M.; Date curation, Q.S.; Investigation, Z.W.; Project administration, G.G. All authors have read and agreed to the published version of the manuscript.

Funding: This research was supported by 111 Project (B17034) Innovative Research Team Development Program of Ministry of Education of China (IRT_17R83), the Guiding Project of Hubei Provincial Department of Education (B2021330), and Open project of Hubei Key Laboratory of Power System Design and Test for Electrical Vehicle granted No.14.

Data Availability Statement: Data cannot be obtained due to privacy.

Conflicts of Interest: The authors declare no conflict of interest.

References

1. Guo, G.; Su, Q. Cycling stability of Fe_2O_3 nanosheets as supercapacitor sheet electrodes enhanced by MgFe_2O_4 nanoparticles. *RSC Adv.* **2023**, *6*, 3643–3651. [[CrossRef](#)] [[PubMed](#)]
2. Wang, G.; Yu, M.; Feng, X. Carbon materials for ion-intercalation involved rechargeable battery technologies. *Chem. Soc. Rev.* **2021**, *50*, 2388–2443. [[CrossRef](#)] [[PubMed](#)]
3. Reddy, G.R.; Dillip, G.R.; Sreekanth, T.V.M.; Rajavaram, R. Mechanistic investigation of defect-engineered, non-stoichiometric, and Morphology-regulated hierarchical rhombus-/spindle-/peanut-like ZnCo_2O_4 microstructures and their applications toward high-performance supercapacitors. *Appl. Surf. Sci.* **2020**, *529*, 147123. [[CrossRef](#)]
4. Sethi, M.; Shenoy, U.S.; Muthu, S.; Bhat, D.K. Facile solvothermal synthesis of NiFe_2O_4 nanoparticles for high-performance supercapacitor applications. *Front. Mater. Sci.* **2020**, *14*, 120–132. [[CrossRef](#)]
5. Kumar, A.; Rathore, H.M.; Sarkar, D.; Shukla, A. Nanoarchitected transition metal oxides and their composites for supercapacitors. *Electrochem. Sci. Adv.* **2021**, *2*, e2100187. [[CrossRef](#)]
6. Dillip, G.R.; Banerjee, A.N.; Anitha, V.C.; Deva, B.; Raju, P.; Joo, S.W.; Min, B.K. Oxygen vacancy-induced structural, optical, and enhanced supercapacitive performance of zinc oxide anchored graphitic carbon nanofiber hybrid electrodes. *ACS Appl. Mater. Interfaces* **2016**, *8*, 5025–5039. [[CrossRef](#)] [[PubMed](#)]
7. Reddy, G.R.; Kumar, N.S.; Raju, B.D.P.; Shanmugam, G.; Al-Ghurabi, E.H.; Asif, M. Enhanced supercapacitive performance of higher-ordered 3d-hierarchical structures of hydrothermally obtained ZnCo_2O_4 for energy storage devices. *Nanomaterials* **2020**, *10*, 1206. [[CrossRef](#)]
8. Guo, C.; Yin, M.; Wu, C.; Li, J.; Sun, C.; Jia, C. Highly stable gully-network Co_3O_4 nanowire arrays as battery-type electrode for outstanding supercapacitor performance. *Front. Chem.* **2018**, *6*, 636. [[CrossRef](#)]
9. Attia, S.Y.; Mohamed, S.G.; Barakat, Y.F.; Hassan, H.H.; Zoubi, W.A. Supercapacitor electrode materials: Addressing challenges in mechanism and charge storage. *Rev. Inorg. Chem.* **2022**, *42*, 53–88. [[CrossRef](#)]
10. Schütter, C.; Pohlmann, S.; Balducci, A. Industrial requirements of materials for electrical double layer capacitors: Impact on current and future applications. *Adv. Energy Mater.* **2019**, *9*, 1900334. [[CrossRef](#)]

11. Fleischmann, S.; Mitchell, J.B.; Wang, R.; Zhan, C.; Jiang, D.E.; Presser, V.; Augustyn, V. Pseudocapacitance: From fundamental understanding to high power energy storage materials. *Chem. Rev.* **2020**, *120*, 6738–6782. [[CrossRef](#)] [[PubMed](#)]
12. Tan, H.T.; Sun, W.; Wang, L.; Yan, Q. 2D transition metal oxides/hydroxides for energy-storage applications. *ChemNanoMat* **2016**, *2*, 562–577. [[CrossRef](#)]
13. Yang, Z.; Cheng, Q.; Li, W.; Li, Y.; Yang, C.; Tao, K. Construction of 2D ZIF-derived hierarchical and hollow NiCo-LDH “nanosheet-on-nanosheet” arrays on reduced graphene oxide/Ni foam for boosted electrochemical energy storage. *J. Alloys Compd.* **2021**, *850*, 156864. [[CrossRef](#)]
14. Wang, Y. Polypyrrole-encapsulated Fe₂O₃ nanotube arrays on a carbon cloth support: Achieving synergistic effect for enhanced supercapacitor performance. *Electrochim. Acta* **2021**, *386*, 138486. [[CrossRef](#)]
15. Kumar, R. Microwave-assisted synthesis of Mn₃O₄-Fe₂O₃/Fe₃O₄@rGO ternary hybrids and electrochemical performance for supercapacitor electrode. *Diam. Relat. Mater.* **2020**, *101*, 107622. [[CrossRef](#)]
16. Simon, P.; Gogotsi, Y. Materials for electrochemical capacitors. *Nat. Mater.* **2008**, *7*, 845–854. [[CrossRef](#)] [[PubMed](#)]
17. Dar, M.A.; Dinakaran, S.; Govindarajan, D.; Ahamed, S.R.; Habib, F.; Siva, C.; Moholkar, A.V.; Ahmad, Z.; Yattoo, M.A. Snx-0MnxS nanomaterial based electrodes for future-generation supercapacitor and data storage devices. *J. Alloys Compd.* **2023**, *958*, 170523. [[CrossRef](#)]
18. Yuan, Y.; Zhou, J.; Rafiq, M.I.; Dai, S.M.; Tang, J.; Tang, W.H. Growth of ni-mn layered double hydroxide and polypyrrole on bacterial cellulose nanofibers for efficient supercapacitors. *Electrochim. Acta* **2019**, *295*, 82–91. [[CrossRef](#)]
19. Ma, L.T.; Fan, H.Q.; Wei, X.Y.; Chen, S.M.; Hu, Q.Z.; Liu, Y. Towards high areal capacitance, rate capability, and tailorable supercapacitors: Co₃O₄@polypyrrole core-shell nanorod bundle array electrodes. *J. Mater. Chem. A* **2018**, *6*, 19058–19065. [[CrossRef](#)]
20. Das, A.K.; Sahoo, S.; Arunachalam, P.; Zhang, S.; Shim, J.J. Facile synthesis of Fe₃O₄ nanorod decorated reduced graphene oxide (RGO) for supercapacitor application. *RSC Adv.* **2016**, *6*, 107057. [[CrossRef](#)]
21. Wang, T.; Chen, H.C.; Yu, F.; Zhao, X.S.; Wang, H.X. Double-shelled hybrid MgFe₂O₄/Fe₂O₃ hollow microspheres as a high-capacity anode for lithium-ion batteries. *J. Ind. Eng. Chem.* **2022**, *110*, 262–273.
22. Nandi, D.; Mohan, V.B.; Bhowmick, A.K. Metal/metal oxide decorated graphene synthesis and application as supercapacitor: A review. *J. Mater. Sci.* **2020**, *55*, 6375–6400. [[CrossRef](#)]
23. Brousse, T.; Bélanger, D.; Long, J.W. To Be or Not To Be Pseudocapacitive. *J. Electrochem. Soc.* **2015**, *162*, A5185–A5189. [[CrossRef](#)]
24. Pan, Y.; Zhang, Y.; Wei, X.; Yuan, C.; Yin, J.; Cao, D.; Wang, G. MgFe₂O₄ nanoparticles as anode materials for lithium-ion batteries. *Electrochim. Acta* **2013**, *109*, 89–94. [[CrossRef](#)]
25. Wang, J.; Zhou, H.; Nanda, J.; Braun, P.V. Three-dimensionally mesostructured Fe₂O₃ electrodes with good rate performance and reduced voltage hysteresis. *Chem. Mater.* **2015**, *27*, 2803–2811. [[CrossRef](#)]
26. Liu, H.; Liu, X.; Wang, S.; Liu, H.K.; Li, L. Transition metal based battery-type electrodes in hybrid supercapacitors: A review. *Energy Storage Mater.* **2020**, *28*, 122–145. [[CrossRef](#)]
27. Gao, W.; Li, Y.; Zhao, J.; Zhang, Z.; Tang, W.; Wang, J.; Wu, Z.; Li, Z. Design and Preparation of Graphene/Fe₂O₃ Nanocomposite as Negative Material for Supercapacitor. *Chem. Res. Chin. Univ.* **2022**, *38*, 1097–1104. [[CrossRef](#)]
28. Liu, W.; Zhu, M.; Liu, J.; Li, X.; Liu, J. Flexible asymmetric supercapacitor with high energy density based on optimized MnO₂ cathode and Fe₂O₃ anode. *Chin. Chem. Lett.* **2019**, *30*, 750–756. [[CrossRef](#)]
29. Zhang, Y.; Lin, R.; Fu, Y.; Wang, X.; Yu, X.; Li, J.; Zhu, Y.; Tan, S.; Wang, Z. Metal-organic framework derived Fe₂O₃ nanocubes on intertwined N-doped carbon nanowires for fiber-shaped supercapacitor. *Mater. Lett.* **2018**, *228*, 9–12. [[CrossRef](#)]
30. Zhu, X.; Zhu, Y.; Murali, S.; Stoller, M.D.; Ruoff, R.S. Nanostructured reduced graphene oxide/Fe₂O₃ composite as a high-performance anode material for lithium ion batteries. *ACS Nano* **2011**, *5*, 3333–3338. [[CrossRef](#)]
31. Zhang, M.; Sha, J.; Miao, X.; Liu, E.; Shi, C.; Li, J.; He, C.; Li, Q.; Zhao, N. Three-dimensional graphene anchored Fe₂O₃@C core-shell nanoparticles as supercapacitor electrodes. *J. Alloys Compd. Interdiscip. J. Mater. Sci. Solid-State Chem. Phys.* **2017**, *696*, 956–963. [[CrossRef](#)]
32. Guo, R.; Dang, L.; Liu, Z.; Lei, Z. Incorporation of electroactive NiCo₂S₄ and Fe₂O₃ into graphene aerogel for high-energy asymmetric supercapacitor. *Colloids Surf. A Physicochem. Eng. Asp.* **2020**, *602*, 125110. [[CrossRef](#)]

Disclaimer/Publisher’s Note: The statements, opinions and data contained in all publications are solely those of the individual author(s) and contributor(s) and not of MDPI and/or the editor(s). MDPI and/or the editor(s) disclaim responsibility for any injury to people or property resulting from any ideas, methods, instructions or products referred to in the content.